Turbulence Characterisation of High-Velocity Free-Surface Flows

Hubert Chanson and Giovanna Carosi

The University of Queensland, Div. of Civil Engineering,
Brisbane Qld 4072, Australia
E-mail: h.chanson@uq.edu.au

Keywords: air-water free-surface flows, high-velocity flows, turbulence, turbulent integral length scales, correlation analysis, signal processing, phase-detection probes, self-similarity

Abstract

In high-velocity free-surface flows, air is continuously being trapped and released through the free-surface. Such high-velocity highly-aerated flows cannot be studied numerically because of the large number of relevant equations and parameters. Herein an advanced signal processing of traditional single- and dual-tip conductivity probes provides some new information on the air-water turbulent time and length scales. The technique is applied to turbulent open channel flows in a large-size facility. The auto- and cross-correlation analyses yield some characterisation of the large eddies advecting the bubbles. The transverse integral turbulent length and time scales are related to the step height: i.e., $L_{xy}/h \sim 0.02$ to 0.2, and $T \times \sqrt{g/h} \sim 0.004$ to 0.04. The results are irrespective of the Reynolds numbers. The present findings emphasise that turbulent dissipation by large-scale vortices is a significant process in the intermediate zone between the spray and bubbly flow regions ($0.3 < C < 0.7$). Some self-similar relationships were observed systematically at both macroscopic and microscopic levels. The results are significant because they provide a picture general enough to be used to characterise the air-water flow field in prototype spillways.

Introduction

In high-velocity open channel flows, the strong interactions between the turbulent waters and the atmosphere lead to some air-water mixing at the interface with the apparition of "white waters". Through the air-water interface, air is continuously being trapped and released, and the resulting air-water mixture may extend to the entire flow (Fig. 1). Herein air bubble entrainment is defined as the entrainment or entrapment of un-dissolved air bubbles and air pockets that are advected within the flowing waters. The term air bubble is used broadly to describe a volume of air surrounded continuously or not within some air-water interface(s). In high-velocity free-surface flows, the resulting air-water mixture is complicated (Rao and Kobus 1971, Wood 1991, Chanson 1997). The void fraction ranges from 100% above the "free-surface" to some small, often non-zero value close to the invert (e.g. Cain and Wood 1981b).

Air bubble entrainment occurs when the turbulent shear stress is large enough to overcome both surface tension and buoyancy effects (if any). In civil engineering applications, the flow velocity exceeds typically 5 to 10 m/s, the flow Reynolds number ranges from 1 E+7 to over 1 E+9 in large dam spillways, and free-surface aeration is nearly always observed (Fig. 1). Such high-velocity highly-aerated flows cannot be studied analytically or numerically because of the large number of relevant equations and parameters. Current knowledge relies upon physical modelling and experimental measurements. Accurate measurement systems for air-water flow measurements are limited to intrusive phase-detection probes, hot-film probes, and LDA/PDA systems. Authoritative reviews include Jones and Delhaye (1976), Cain and Wood (1981a), Chanson (1997,2002) and Chang et al. (2003).

(A) Chute Montmorency, Québec, Canada on 6 June 2004 (Fall height: 83 m, shutter speed: 1/800 s)

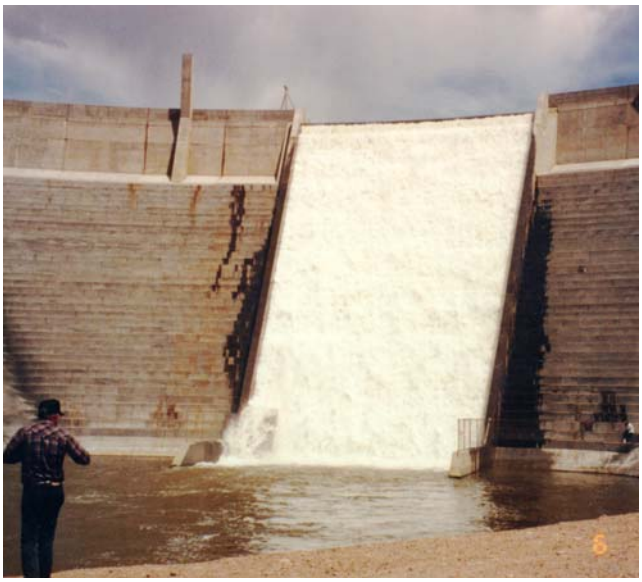

(B) Stepped spillway of Santa Cruz dam, New Mexico, USA (Courtesy of John LaBoon and USBR)

Figure 1: Photographs of "white waters" in high-velocity free-surface flows.

In the present study, it is shown that an advanced signal processing of traditional single- and dual-tip conductivity probes may provide new information on the air-water turbulent time and length scales. The technique was applied to turbulent open channel flows in a large-size facility under controlled flow conditons. Detailed air-water flow properties were recorded systematically for several flow rates including turbulence levels and turbulent time and length scales.

Nomenclature

C	void fraction (time-averaged void fraction)
C_{mean}	depth-averaged void fraction: $C_{mean} = \frac{1}{Y_{90}} \times \int_{y=0}^{Y_{90}} C \times dy$
C	instantaneous void fraction (C = 0 or 1)
D_H	hydraulic diameter (m)
D_o	dimensionless coefficient
d	equivalent clear water depth (m): $d = \int_{y=0}^{Y_{90}} (1-C) \times dy$
d_c	critical flow depth (m): $d_c = \sqrt[3]{q_w^2/g}$
F	bubble count rate (Hz)
F_{max}	maximum bubble count rate (Hz) in a cross-section
g	gravitational constant (m/s^2)
h	vertical step height (m)
K'	dimensionless constant
L_I	longitudinal distance (m) between the chute crest and the inception point of free-surface aeration
L_{xx}	advective integral length scale (m) of the air-water flow
L_{xy}	transverse integral length scale (m) of the air-water flow
Q_w	water discharge (m^3/s)
q_w	water discharge per unit width (m^2/s)
R	normalised coefficient of correlation
Re	flow Reynolds number: $Re = \frac{\rho_w \times U_w \times D_H}{\mu_w}$
R_{xx}	normalised auto-correlation function
R_{xy}	normalised cross-correlation function
T	characteristic time lag (s) for which the cross-correlation function is maximum
$T_{0.5}$	characteristic time for which the normalised auto-correlation function equals: $R_{xx}(T_{0.5}) = 0.5$
Tu	turbulent intensity : $Tu = v_x'/V$
T	transverse/streamwise integral time scale of the large eddies advecting air bubbles
U_w	flow velocity (m/s) defined as $U_w = q_w/d$
V	air-water velocity (m/s)
V_c	critical flow velocity (m/s) : $V_c = \sqrt{g \times d_c}$
V_{90}	characteristic velocity (m/s) where C = 0.90
v_x'	root mean square of the longitudinal velocity variance (m/s)
v_y'	root mean square of the normal velocity variance (m/s)
v_z'	root mean square of the transverse velocity variance (m/s)
W	channel width (m)
x	longitudinal distance (m) from the spillway crest
Y	probe sensor separation distance (m)
Y90	characteristic air-water depth where C = 0.90
y	distance (m) normal from the pseudo-bottom formed by the step edges
y'	dimensionless distance $y' = y/Y_{90}$
z	transverse distance (m) from the channel centreline)

Greek letters

Δx	longitudinal probe sensor separation distance (m)
Δz	transverse probe sensor separation distance (m)
μ	viscosity (Pas)
ρ	density (kg/m^3)
θ	angle between the horizontal and the pseudo-bottom formed by the step edges
σ	surface tension (N/m) between air and water
τ	time lag (s)
$\tau_{0.5}$	time scale for which the cross-correlation function is half of its maximum value: $R_{xy}(T+\tau_{0.5}) = 0.5 \times R_{xy}(T)$

Subscripts

air	air properties
c	critical flow conditions
max	maximum value in the cross-section
w	water properties

Experimental Facility and Instrumentation

New experiments were performed in the Gordon McKay Hydraulics Laboratory at the University of Queensland (Table 1, Fig. 2). The experimental channel was previously used by Chanson and Toombes (2002a) and Gonzalez (2005). The waters were supplied from a large feeding basin (1.5 m deep, surface area 6.8 m × 4.8 m) leading to a sidewall convergent with a 4.8:1 contraction ratio. The pump, delivering the flow rate, was controlled with an adjustable frequency AC motor drive which enabled an

accurate discharge adjustment in the closed-circuit system.
The test section consisted of a broad-crested weir (1 m wide, 0.6 m long) followed by ten identical steps (h = 0.1 m, l = 0.25 m) made of marine ply (Fig. 2). The stepped chute was 1 m wide with perspex sidewalls followed by a horizontal concrete-invert canal ending in a dissipation pit. Further details on the experimental facility and data were reported in Carosi and Chanson (2006).

Table 1: Experimental flow conditions.

	q_w (m^2/s)	d_c/h $\sqrt[3]{\frac{Q_w^2}{g \times W^2 \times h^3}}$	Re $\frac{\rho_w \times U_w \times D_H}{\mu_w}$	Remarks
Present study	0.095	1.0	3.8 E+5	W = 1 m. Single-tip probes
	0.116	1.15	4.6 E+5	
	0.143	1.33	5.7 E+5	
	0.161	1.45	6.4 E+5	
	0.180	1.57	7.1 E+5	
	0.116	1.15	4.6 E+5	Double-tip probe
	0.143	1.33	5.7 E+5	
	0.161	1.45	6.4 E+5	

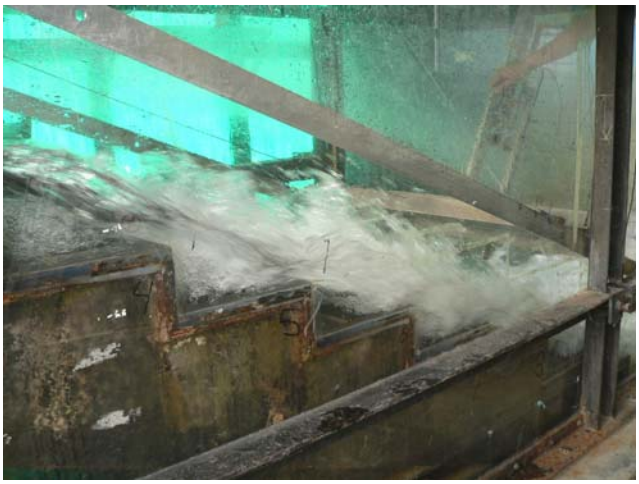

Figure 2: Photograph of the test section for d_c/h = 1.0, Re = 3.8 E+5 (shutter speed: 1/80 s).

Instrumentation

Clear-water flow depths were measured with a point gauge. The water discharge was measured from the upstream head above the crest, and the head-discharge relationship was checked with detailed velocity distribution measurements on the crest itself (Gonzalez 2005).
Air-water flow properties were measured with single-tip and double-tip conductivity probes (Fig. 3 and 4). Basic air-water flow measurements were performed with single-tip conductivity probes (Fig. 3). The probe sensor consisted of a sharpened rod (∅ = 0.35 mm) coated with non-conductive epoxy set into a stainless steel surgical needle acting as the second electrode. Additional measurements were performed with a double-tip conductivity probe (Fig. 4). The sensors consisted of a platinum wire (∅ = 0.25 mm) insulated except for its tip and set into a metal supporting tube. The probe sensors were aligned in the flow direction. The leading tip had a small frontal area (i.e. 0.05 mm^2) and the trailing tip was laterally offset by 1.4 mm to avoid wake disturbance from the first tip. The longitudinal spacing between probe sensors was measured with a microscope and this yielded Δx = 7.0 mm.

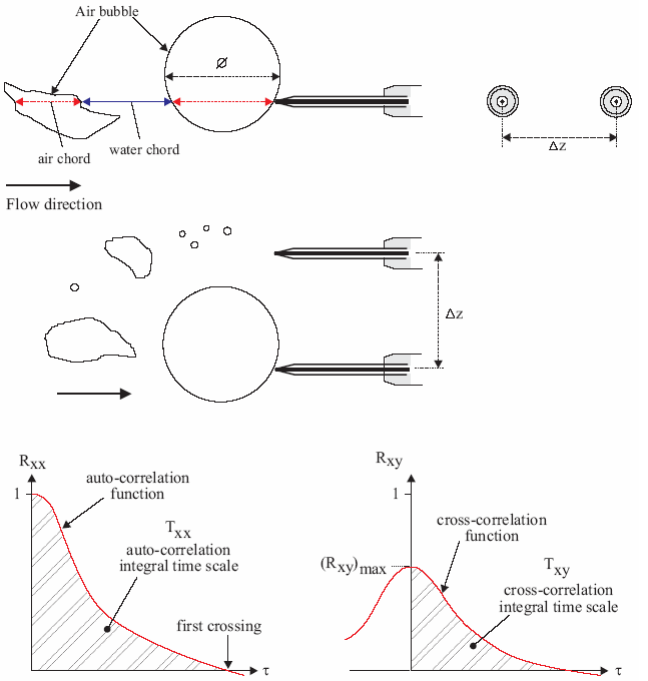

Figure 3: Sketch a single-tip intrusive phase-detection probe.

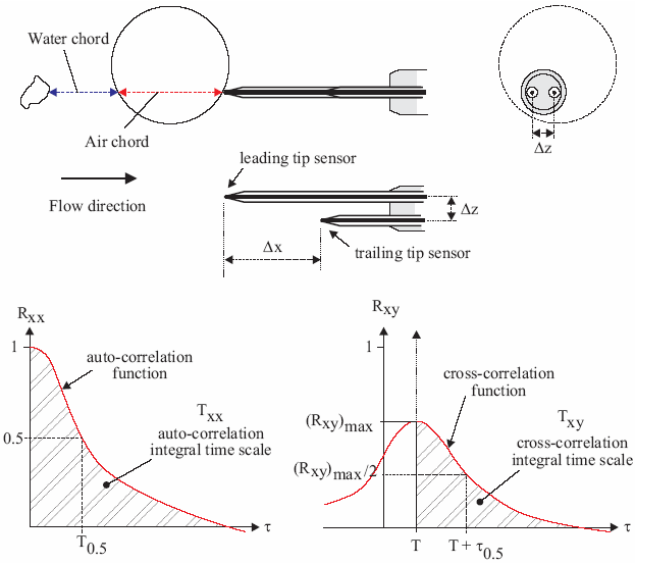

Figure 4: Sketch a double-tip intrusive phase-detection probe.

All the probes were excited by an electronic system (Ref. UQ82.518) designed with a response time less than 10 µs and calibrated with a square wave generator. The probe sensors were scanned at 20 kHz per sensor for 45 seconds at each sampling position.
Herein the measurements were conducted on the channel centreline (z = 0). For some experiments, a second, identical probe was placed beside the first one with the probe sensors at the same vertical and streamwise distances y and x respectively. The reference probe was located on the channel centreline (z = 0) while the second probe was separated in the transverse direction by a known separation Δz (Fig. 3).

Signal Processing and Analysis

The measurement principle of phase-detection intrusive probes is based upon the difference in optical index or electrical resistivity between air and water. The intrusive probe sensor is designed to pierce the bubbles and droplets. That is, the probe sensor must be sharpened and it must ideally face the stream of incoming bubbles as shown in Figures 3 and 4. The signal processing may be conducted on the raw signal output (e.g. Fig. 5) and on a thresholded "square wave" signal.

A thresholded signal analysis relies upon some arbitrary discrimination between the two phases. The technique may be based upon single or multiple thresholds, or some signal pattern recognition. The resulting square-wave signal yields the instantaneous void fraction c : $c = 0$ in water and $c = 1$ in air. It is used to calculate the time-averaged void fraction C, the bubble count rate F, the air/water chord times, the bubble/droplet chord lengths and their statistical moments (mean, median, std, skewness, kurtosis), and the streamwise particle grouping analysis. In high-velocity free-surface flows, the most robust discrimination technique is the single threshold technique with a threshold set at about 45 to 55% of the air-water voltage range (Herringe and Davis 1974, Toombes 2002, Carosi and Chanson 2006).

The signal processing of the raw probe outputs is typically used for some correlation analyses. These yield the time-averaged interfacial velocity, the turbulence intensity, the auto-correlation and cross-correlation integral time and length scales, the air-water integral length and time scales (see below). A further level of signal analysis is the spectral analyses (Chanson and Gonzalez 2004, Gonzalez 2005).

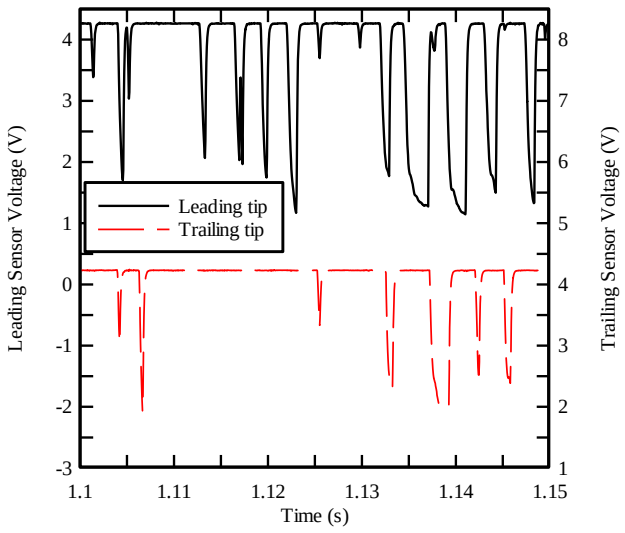

Figure 5: Probe signal outputs of the double-tip conductivity probe (Δx = 7.0 mm) in skimming flow: d_c/h = 1.33, Re = 5.7 E+5, y = 0.0365 m, C = 0.187, F = 167 Hz.

Basic signal analysis

The time-averaged void fraction C is the proportion of time that the probe tip is in the air. Although past experiences showed that the probe orientation with the flow direction had little effect on the void fraction accuracy, the phase-detection probes are designed to pierce the bubbles/droplets with minimum interference and the probe sensor should face the bubbles/droplets as sketched in Figures 3 and 4.

The bubble count rate F is the number of bubbles impacting the probe tip per second. Note the relationship between bubble count rate and void fraction. Experimental data showed a pseudo-parabolic relationship:

$$\frac{F}{F_{max}} = 4 \times C \times (1 - C) \quad (1)$$

where F_{max} is the maximum bubble frequency. Toombes (2002) demonstrated the theoretical validity and he proposed a more general extension (Toombes 2002, pp. 190-195). Another reasoning suggests that the bubble count rate is proportional to the fluctuations of the instantaneous void fraction c. Simple considerations show that its variance c_{rms}^2 equals C×(1-C) where C is the time-averaged void fraction. Hence the bubble count rate must satisfy:

$$F \equiv c_{rms}^2 = C \times (1 - C) \quad (2)$$

Correlation analyses

When two or more phase detection probe sensors are simultaneously sampled, some correlation analyses may provide additional information on the bubbly flow structure. A well-known application is the use of dual tip probe to measure the interfacial velocity (Fig. 4). A cross-correlation analysis between the two probe sensors yields the time averaged velocity:

$$V = \frac{\Delta x}{T} \quad (3)$$

where T is the air-water interfacial travel time for which the cross-correlation function is maximum and Δx is the longitudinal distance between probe sensors (Fig. 4). Turbulence levels may be further derived from the relative width of the cross-correlation function:

$$Tu = 0.85 \times \frac{\sqrt{\tau_{0.5}^2 - T_{0.5}^2}}{T} \quad (4)$$

where $\tau_{0.5}$ is the time scale for which the cross-correlation function is half of its maximum value such as: $R_{xy}(T + \tau_{0.5}) = 0.5 \times R_{xy}(T)$, R_{xy} is the normalised cross-correlation function, and $T_{0.5}$ is the characteristic time for which the normalised auto-correlation function equals : $R_{xx}(T_{0.5}) = 0.5$ (Fig. 4). Physically, a thin narrow cross-correlation function ($(\tau_{0.5}-T_{0.5})/T << 1$) must correspond to little fluctuations in the interfacial velocity, hence a small turbulence level Tu. While Equation (4) is not the true turbulence intensity v_x'/V, it is an expression of some turbulence level and average velocity fluctuations (Chanson and Toombes 2002).

More generally, when two probe sensors are separated by a transverse or longitudinal distance Y, their signals may be analysed in terms of the auto-correlation and cross-correlation functions R_{xx} and R_{xy} respectively. Figure 3 shows two probe sensors separated by a transverse distance Y = Δz. Practically the original data set must be segmented because the periodogram resolution is inversely proportional to the number of samples and it could be biased with large data sets (Hayes 1996). Basic correlation analysis results include the maximum cross-correlation coefficient $(R_{xy})_{max}$, and the auto- and cross-correlation time

scales T_{xx} and T_{xy} where :

$$T_{xx} = \int_{\tau=0}^{\tau=\tau(R_{xx}=0)} R_{xx}(\tau) \times d\tau \quad (5)$$

$$T_{xy} = \int_{\tau=0}^{\tau=\tau(R_{xy}=0)} R_{xy}(\tau) \times d\tau \quad (6)$$

where R_{xx} is the normalised auto-correlation function, τ is the time lag, and R_{xy} is the normalised cross-correlation function between the two probe output signals (Fig. 3). The auto-correlation time scale T_{xx} represents the integral time scale of the longitudinal bubbly flow structure. It is a characteristic time of the eddies advecting the air-water interfaces in the longitudinal direction. The cross-correlation time scale T_{xy} is a characteristic time of the vortices with a length scale Y advecting the air-water flow structures. The length scale Y may be a transverse separation distance Δz (Fig. 3) or a streamwise separation Δx (Fig. 4).

When identical experiments with two probes are repeated using different separation distances Y (Y = Δz or Δx), an integral turbulent length scale may be calculated as :

$$L_{xy} = \int_{Y=0}^{Y=Y((R_{xy})_{max}=0)} (R_{xy})_{max} \times dY \quad (7)$$

The length scale L_{xy} represents a measure of the transverse/streamwise length scale of the large vortical structures advecting air bubbles and air-water packets.

An advective integral length scale is $L_{xx} = V \times T_{xx}$.

A turbulence integral time scale is:

$$\mathbf{T} = \frac{1}{L_{xy}} \times \int_{Y=0}^{Y=Y((R_{xy})_{max}=0)} (R_{xy})_{max} \times T_{xy} \times dY \quad (8)$$

T represents the transverse/streamwise integral time scale of the large eddies advecting air bubbles.

Basic Air-Water Flow Patterns

In the stepped chute, the basic flow regimes were inspected in a series of visual observations with discharges ranging from 0.008 to 0.180 m^3/s. A nappe flow regime was observed for small flow rates ($d_c/h < 0.5$), where d_c is the critical flow depth and h is the vertical step height. The waters flowed as a succession of free-falling nappes and the flow pattern was consistent with the early observations of Horner (1969), Chamani and Rajaratnam (1994), and Chanson (1994). For some intermediate discharges ($0.5 < d_c/h < 0.95$), the flow had a chaotic behaviour that is characteristic of a transition flow regime. These intermediate flows were characterised by a chaotic motion (Ohtsu and Yasuda 1997, Chanson and Toombes 2004). For larger flows ($d_c/h > 0.95$), the waters skimmed above the pseudo-bottom formed by the step edges. In the skimming flow regime, the waters were non-aerated at the upstream end of the chute (Fig. 6). Free-surface aeration occurred because the turbulent shear next to the free-surface became larger than the bubble resistance offered by surface tension and buoyancy. Downstream of the inception point of free-surface aeration, some strong air-water mixing took place as illustrated in Figures 2 and 6. Large amounts of air were entrained, and very-strong interactions between main stream turbulence, step cavity recirculation zones and free-surface were observed associated with strong energy dissipation and flow resistance

In transition and skimming flows, the location of the inception point of free-surface aeration was recorded with discharges per unit width larger than 0.034 m^2/s. The data were compared successfully with earlier studies (Chanson 1995,2001, Chanson and Toombes 2002). For the present study, the results were best correlated by :

$$\frac{L_I}{h \times \cos\theta} = 1.05 + 5.11 \times \frac{q_w}{\sqrt{g \times \sin\theta \times (h \times \cos\theta)^3}} \quad 0.45 < d_c/h < 1.6 \quad (9)$$

with a normalised correlation coefficient of 0.95, where q_w is the water discharge per unit width, g is the gravity acceleration, and θ is the average chute slope (Fig. 6). Equation (9) is valid for transition and skimming flows on the 22º stepped chute only.

Overall the present results were very-close to the earlier observations of Chanson and Toombes (2002) and Gonzalez (2005) in the same chute.

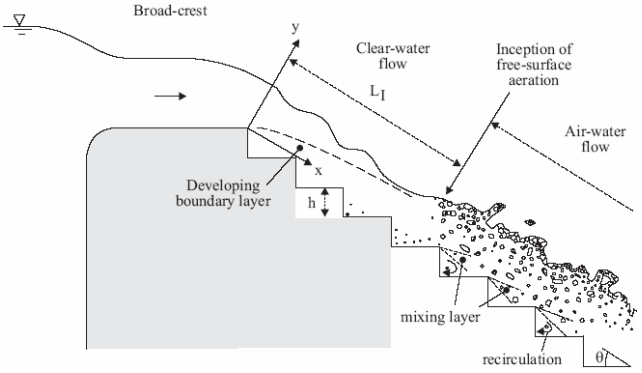

Figure 6: Sketch of a skimming flow on a stepped channel.

Air-Water Flow Characteristics

Void fraction and bubble count rate distributions

Experimental observations demonstrated some substantial free-surface aeration immediately downstream of the inception point of free-surface aeration and the flow aeration was sustained downstream (Fig. 1, 2 & 7). At the step edges, the advective diffusion of air bubbles was described by an analytical model of air bubble diffusion:

$$C = 1 - \tanh^2\left(K' - \frac{y'}{2 \times D_o} + \frac{\left(y' - \frac{1}{3}\right)^3}{3 \times D_o}\right) \quad (10)$$

where C is the void fraction, $y' = y/Y_{90}$, y is distance measured normal to the pseudo-invert, Y_{90} is the characteristic distance where C = 90% (Chanson and Toombes 2002). K' is an integration constant and D_o is a function of the mean void fraction C_{mean} only :

$$K' = 0.32745 + 12 \times D_o - 881 \times D_o \quad (11)$$

$$C_{mean} = 0.762 \times (1.0434 - \exp(-3.614 \times D_o)) \quad (12)$$

Equation (10) is compared with some experimental data in Figure 7. Figure 7 presents an example of dimensionless distributions of void fraction and bubble count rate $F \times d_c/V_c$ as functions of y/d_c at several step edges for the same flow rate where d_c and V_c are the critical flow depth and velocity respectively. For that discharge, the flow aeration was nil at

step edge 6, immediately upstream of the inception point. Between step edges 6 and 7, some strong self-aeration took place, and the amount of entrained air and the mean air content were about constant between the step edges 7 and 10, with C_{mean} = 0.36 at the last step edge 10.

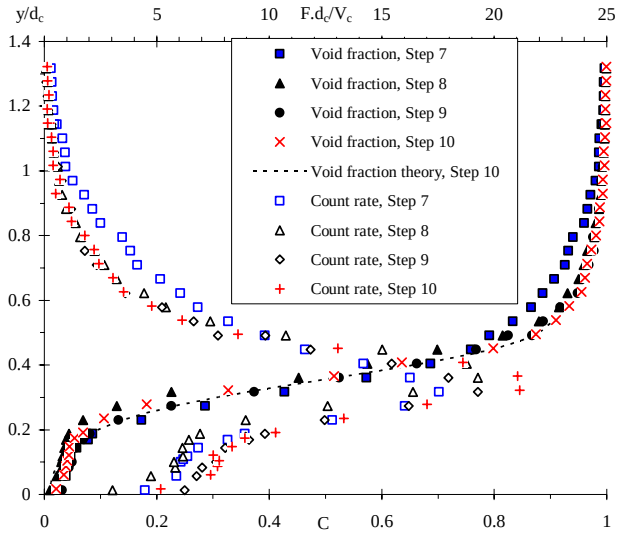

Figure 7: Dimensionless distributions of void fraction C and bubble count rate $F \times d_c/V_c$ for d_c/h = 1.15 (single-tip probe, ∅= 0.35 mm). Comparison with Equation (10) (Step edge 10).

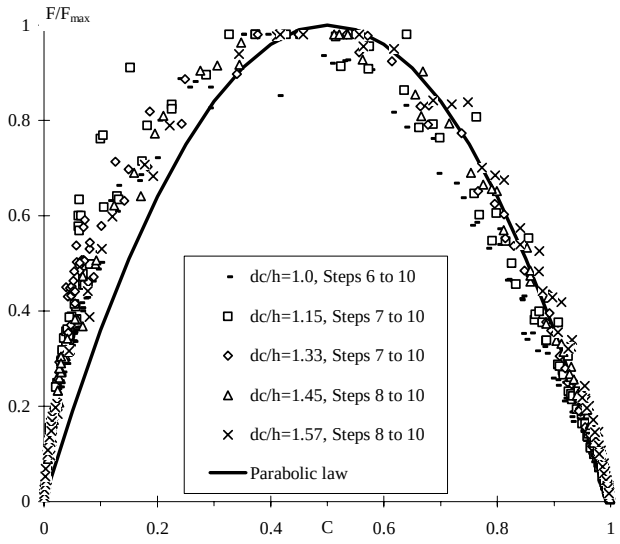

Figure 8: Dimensionless relationship between bubble count rate and void fraction. Comparison with Equation (1).

Figure 7 shows also some typical dimensionless distributions of bubble count rate. The results presented consistently a characteristic shape with a maximum value F_{max} observed for void fractions between 0.36 and 0.60. The relationship between bubble count rate and void fraction provides some useful insight into the bubbly flow structure. Figure 8 presents typical dimensionless relationship between bubble count rate and void fraction at several cross-sections and for several discharges. The data are compared with Equation (1) in Figure 8 and they showed a maximum bubble count rate for $0.36 \leq C \leq 0.60$. A similar pattern was observed in smooth chute and stepped spillway flows (e.g. Chanson 1997b, Chanson and Toombes 2002, Kokpinar 2005).

Air-water velocity and turbulence level distributions

Typical distributions of air-water velocity and turbulence intensity are presented in Figure 5 for one flow rate. At each step edge, the velocity distributions compared favourably with a power-law function for $y/Y_{90} \leq 1$ and with an uniform profile for $y/Y_{90} > 1$:

$$\frac{V}{V_{90}} = y'^{1/N} \qquad 0 \leq y' \leq 1 \quad (13a)$$

$$\frac{V}{V_{90}} = 1 \qquad 1 \leq y' \quad (13b)$$

where V_{90} is the characteristic air-water velocity at $y = Y_{90}$. Several studies yielded Equation (13a) (e.g. Matos 2000, Boes 2000, Chanson and Toombes 2002, Gonzalez and Chanson 2004), but a few documented the velocity distribution in the upper spray region. Equation (13) is compared with experimental data in Figure 9. In the present study, the velocity power law exponent was 1/10 in average (i.e. N = 10), although it varied between adjacent step edges. Such fluctuations were believed to be caused some complicated interference between adjacent shear layers and cavity flows.

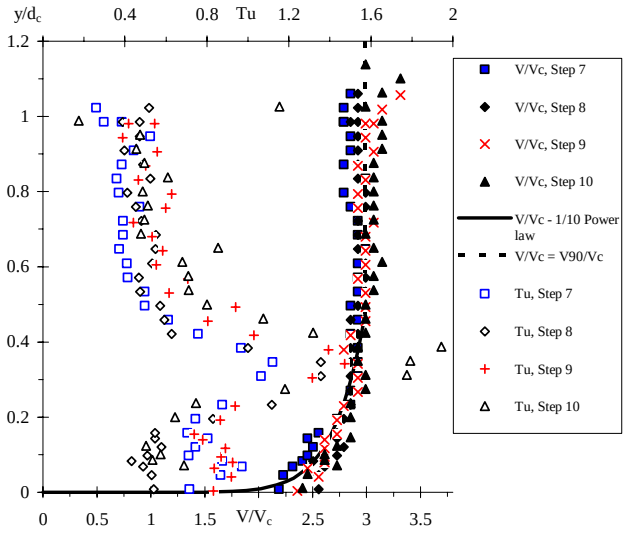

Figure 9: Dimensionless distributions of air-water velocity V/V_c and turbulence intensity Tu for d_c/h = 1.33 (double-tip probe, ∅= 0.25 mm). Comparison with Equation (13) (Step edge 10).

The distributions of turbulence intensity Tu showed high levels of turbulence in the skimming flows : $0.3 \leq Tu \leq 3$ (Fig. 9). The quantitative results were comparable with earlier studies in aerated and non-aerated skimming flows (Chanson and Toombes 2002, Gonzalez and Chanson 2004, Amador et al. 2006).

Herein the turbulence intensity maxima were typically observed for $0.3 \leq y/d_c \leq 0.4$ that corresponded to $0.35 \leq C \leq 0.6$. In that intermediate flow region ($0.3 \leq C \leq 0.6$), the air-water flow structure was extremely complicated; it was dominated by interactions between particles and turbulent shear. It is hypothesised that the high turbulence levels in this intermediate region were caused by the continuous deformations and modification of the air-water interfacial

structure.

Probability distribution functions of bubble and droplet chords

The probability distribution functions of chord sizes were analysed in terms of bubble chords in the bubbly flow (C < 0.3) and in terms of droplet chord lengths in the spray region (C > 0.7). Typical results are presented in Figure 10. For each graph, the legend provides the local air-water flow properties (C, F). The histogram columns represent each the probability of chord sizes in a 0.5 mm chord interval. For example, the probability of bubble chords between 1 and 1.5 mm is represented by the column labelled 1 mm. Chord sizes larger than 15 mm are regrouped in the last column (> 15).

In the bubbly flow region (C < 0.3), the probability distribution functions showed a broad spectrum of bubble chords at each location (Fig. 10A). The range of bubble chord extended from less than 0.3 mm to more than 15 mm. The bubble chord size distributions were skewed with a preponderance of small bubbles relative to the mean. In Figure 10A, the mode of the probability distribution function was observed for chords between 0.5 and 1 mm. The probability distribution functions of bubble chord tended to follow a log–normal distribution at all locations and for all discharges. The result was consistent with the earlier data of Chanson and Toombes (2002) and Gonzalez (2005) in skimming flows.

In the spray region, the probability distribution functions of drop sizes showed also a wide range of droplet chords at each location (Fig. 10B). While the droplet chord size distributions were skewed with a preponderance of small droplets, the probability density function was flatter than that of the bubble chords (Fig. 10). In the upper spray region (C > 0.95), the probability distribution functions were flat and did not follow a log-normal distribution.

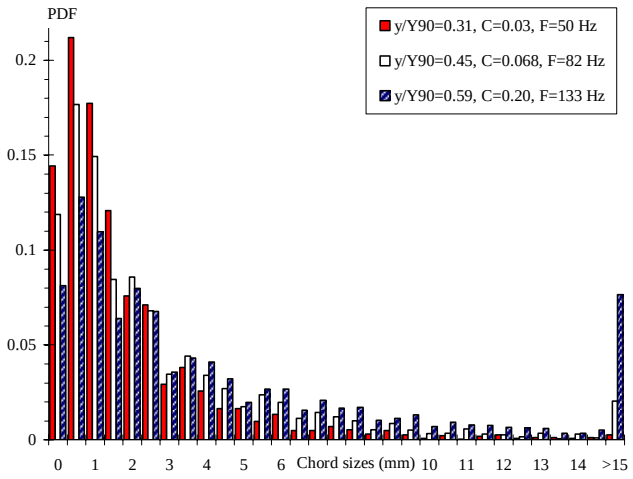

(A) Bubble chord size data (C < 0.3)

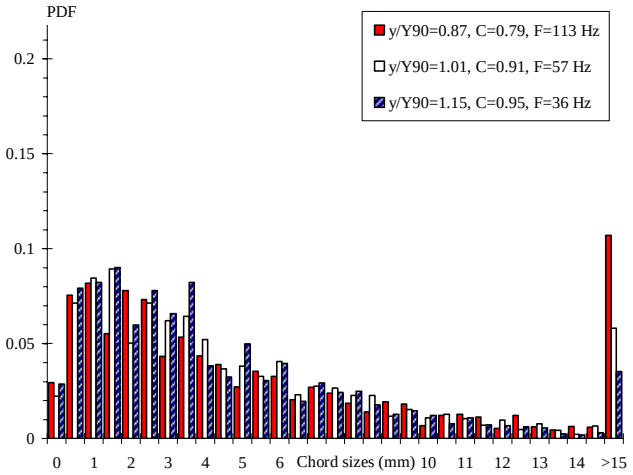

(B) Droplet chord size data (C > 0.7)

Figure 10: Probability distribution functions of chord sizes in skimming flows. Flow conditions: d_c/h = 1.45, Step 10, double-tip probe (∅= 0.25 mm).

Integral Turbulent Time and Length Scales

Some experiments were conducted with two identical sensors separated by a transverse distance Δz and they were repeated for several separation distances (Table 2). Table 2 lists the experimental conditions and summarises some key results. All these measurements were performed with identical single-tip conductivity probes (∅ = 0.35 mm).

Table 2: Experimental observations of maxima of transverse cross-correlation time scale $(T_{xy})_{max}$ and of maximum cross-correlation $(R_{xy})_{max}$ in a cross-section as functions of the transverse separation distance.

d_c/h $\sqrt[3]{\frac{Q_w^2}{g \times W^2 \times h^3}}$	Δz (mm)	$(R_{xy})_{max}$	$(T_{xy})_{max}$ (s)	Remarks
1.15	0	1 ($^+$)	0.0053 ($^+$)	Step edge 10.
	3.6	0.6339	0.005	
	6.3	0.4504	0.0037	
	8.45	0.4293	0.0039	
	10.75	0.3914	0.0038	
	13.7	0.3172	0.0041	
	16.7	0.3215	0.0039	
	21.7	0.2391	0.0027	
	29.5	0.182	0.0023	
	40.3	0.1516	0.0023	
1.45	0	1 ($^+$)	0.0055 ($^+$)	Step edge 10.
	3.6	0.6493	0.0048	
	8.45	0.468	0.0041	
	13.7	0.37	0.0044	
	21.7	0.2845	0.0040	
	40.3	0.1417	0.0020	
	55.7	0.1166	0.0019	

Note: ($^+$) : auto-correlation result.

Typical distributions of auto- and cross-correlation time scale are shown in Figure 11 for three separation distances. Note that the correlation time scales are presented in seconds. The void fraction data are also reported for completeness in Figure 11.

For Δz < 20 mm, the experimental results showed similar

distributions of auto- and cross-correlation time scales in the bulk of the flow (C < 0.9). The auto-correlation time scales T_{xx} (symbols +) exhibited however a different trend in the upper spray region. This is seen in Figure 7 for $y/d_c > 0.8$. It is suggested that the pattern may indicate a change in the spray structure with the upper spray region. For C > 0.95, the spray consisted primarily of ejected droplets that do not interact with the rest of the flow.
For all flow conditions and at each step edge, the distributions of cross-correlation time scale T_{xy} presented a maximum in the intermediate region (0.3 < C < 0.7). Observed maxima of auto- and cross-correlation time scales are reported in Table 2.

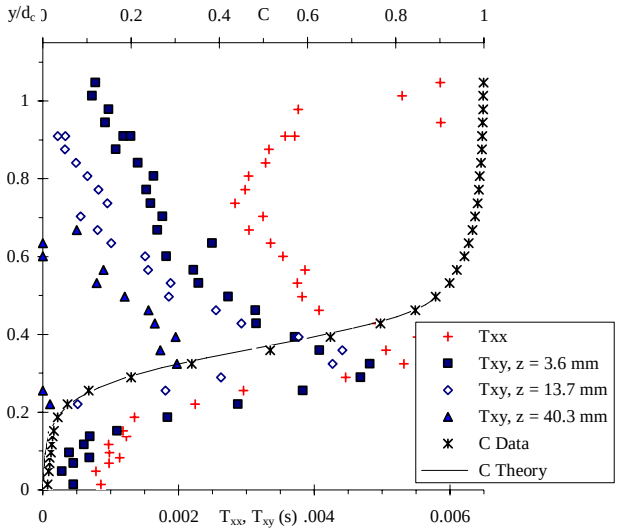

Figure 11: Distributions of auto- and cross-correlation time scales in skimming flows. Comparison with the void fraction distribution. Flow conditions: d_c/h = 1.45, Step 10, single-tip probe (∅= 0.35 mm).

For some experiments which were repeated with several transverse separation distances, the turbulent length and time scales, L_{xy} and $\mathbf{T}$ respectively, were calculated. Typical results in terms of dimensionless turbulent length scales L_{xx}/h and L_{xy}/h, and integral turbulent time scale $\mathbf{T}\times\sqrt{g/h}$, are presented in Figure 12. The measured void fraction data are shown for completeness.
In bubbly flows, the turbulent length scales are closely linked with the characteristic sizes of the large-size eddies entrapping air bubbles. This was demonstrated by some series of high-speed photographs (e.g. Hoyt and Sellin 1989, Chanson 1997). Herein the turbulent length scale L_{xy} characterised the transverse size of the large vortical structures advecting the air bubbles and air-water packets. The integral scales were related to the step height h : i.e., L_{xy}/h = 0.02 to 0.2 (Fig. 12). The result was irrespective of the dimensionless flow rate d_c/h within the relatively limited range of the experiments. The associated turbulence time scale $\mathbf{T}$ is a measure of the integral time scale of the large eddies. Present results yielded basically : $0.004 \leq \mathbf{T}\times\sqrt{g/h} \leq 0.04$.
Figure 13 presents some typical dimensionless relationship between turbulent length scales L_{xx}/h and L_{xy}/h, and integral turbulent time scale $\mathbf{T}\times\sqrt{g/h}$ and the void fraction in a cross-section. Both the integral turbulent length and time scales were maximum for about C = 0.5 to 0.7 (Fig. 12 and 13). The present results highlighted that the relationships between the integral length scales L_{xy} and L_{xx} and integral time scale $\mathbf{T}$, and the void fraction had a skewed parabolic shape with a maxima occurring for void fractions between 0.6 and 0.65 (Fig. 12 & 13). The dimensionless distributions of advection length scale L_{xx}, transverse turbulent length scale L_{xy}, and transverse integral turbulent time scale $\mathbf{T}$ were best correlated by :

$$\frac{L_{xx}}{(L_{xx})_{max}} = 1.6\times C^{0.55}\times(1-C)^{0.30} \qquad C < 0.97 \quad (14)$$

$$\frac{L_{xy}}{(L_{xy})_{max}} = 1.75\times C^{0.57}\times(1-C)^{0.324} \qquad C < 1 \quad (15)$$

$$\mathbf{T}/\mathbf{T}_{max} = 1.97\times C^{0.59}\times(1-C)^{0.50} \qquad C < 0.97 \quad (16)$$

where $(L_{xx})_{max}$, $(L_{xy})_{max}$ and $\mathbf{T}_{max}$ are the characteristic maxima in the cross-section (Table 3). Equation (14) to (16) is compared with experimental data in Figure 13. Note that Equations (14) and (16) are not valid in the upper spray region (C > 0.95 to 0.97).
The present findings emphasised the existence of large-scale turbulent structures in the intermediate zone (0.3 < C < 0.7) between the bubbly flow and spray regions. It is hypothesised that these large vortices may have a preponderant role in terms of turbulent dissipation.

Table 3: Characteristic integral turbulent length and time scales, and advection length scales in skimming flows on a stepped chute.

$\frac{d_c/h}{\sqrt[3]{\frac{Q_w^2}{g\times W^2\times h^3}}}$	$\frac{(L_{xx})_{max}}{Y_{90}}$	$\frac{(L_{xy})_{max}}{Y_{90}}$	$\mathbf{T}_{max}\times\sqrt{\frac{g}{Y_{90}}}$	Remarks
1.15	0.263	0.223	0.0473	C < 0.97
1.45	0.231	0.1865	0.0472	C < 0.97

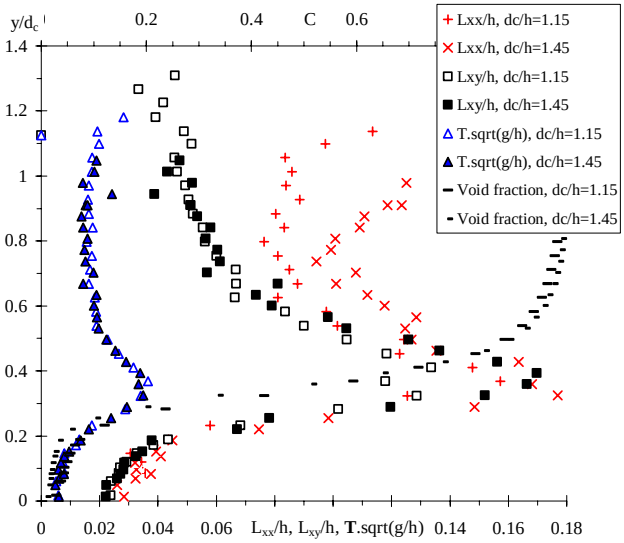

Figure 12: Dimensionless distributions of integral turbulent length scales L_{xx}/h and L_{xy}/h, and transverse integral time scale $\mathbf{T}\times\sqrt{g/h}$ in skimming flows. Comparison with void fraction measurements. Flow conditions: d_c/h = 1.15 & 1.45,

Step 10, single-tip probe (∅= 0.35 mm).

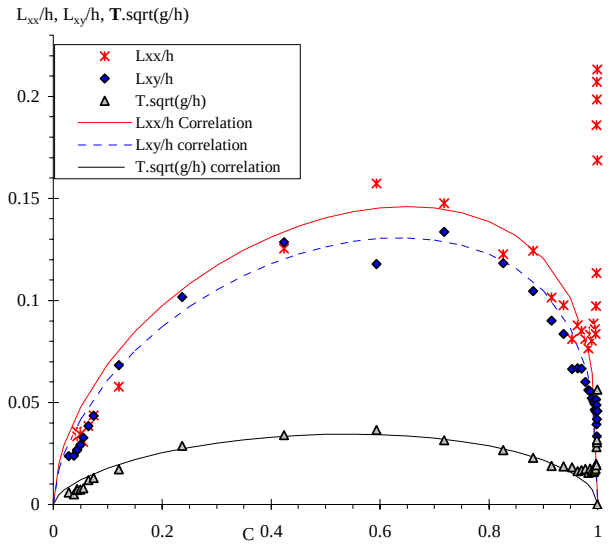

Figure 13: Dimensionless relationship between integral turbulent length scales L_{xx}/h and L_{xy}/h, transverse integral time scale $T\times\sqrt{g/h}$ and void fraction. Flow conditions: d_c/h = 1.15, Step 10, single-tip probe (∅= 0.35 mm).

Relationship between integral scales and turbulent intensity

The present results showed that the intermediate air-water region (0.3 < C < 0.7) between the bubbly and spray regions was characterised by high turbulence intensities, cross-correlation time maxima and the largest integral turbulent time and length scales (Fig. 9, 11, 12 & 13). The findings suggested that some turbulence dissipation by large-scale vortices occurred in the main stream and that it had a significant role in the high-velocity free-surface skimming flows.

On the stepped chute, the turbulent dissipation was associated with a rapid development of the upstream boundary layer (Fig. 6), strong interactions between flow turbulence and free-surface, and some substantial air entrainment downstream of the inception point. The stepped invert contributed to intense turbulence production, and some turbulent energy was dissipated in the form of large-scale vortices in the bulk of the flow.

The present results showed that, in a cross-section, the turbulent intensity Tu and the turbulent integral length and time scales L_{xy}/h and $T\times\sqrt{g/h}$ were closely linked. The turbulence intensity data exhibited a monotonic increase with increasing turbulent time and length scales (Fig. 14). The relationship between turbulence level and turbulent scales were best correlated by:

$$Tu = 0.372\times\exp\left(8.73\times\frac{L_{xy}}{h}\right) \qquad R = 0.754 \quad (17)$$

$$Tu = 0.316\times\exp\left(44.7\times T\times\sqrt{\frac{g}{h}}\right) \qquad R = 0.764 \quad (18)$$

Equations (17) and (18) are compared with experimental data in Figure 14. Despite some scatter, the findings demonstrated some increased turbulence levels with increased large-scale turbulence.

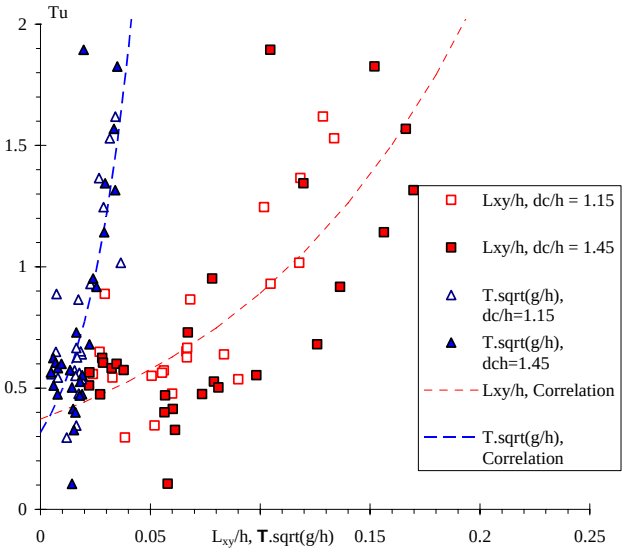

Figure 14: Dimensionless relationship between turbulence intensity and integral turbulent length scale L_{xy}/h and transverse integral time scale $T\times\sqrt{g/h}$ in skimming flows. Flow conditions: d_c/h = 1.15 & 1.45, Step 10, single-tip probe (∅= 0.35 mm).

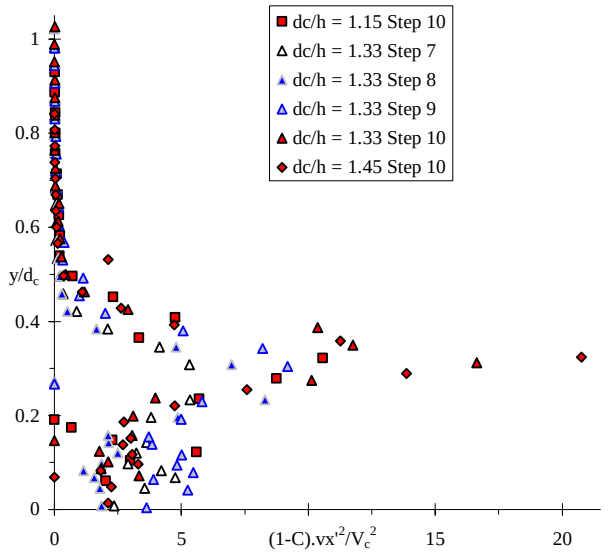

Figure 15: Dimensionless turbulent kinetic energy per unit volume $(1-C)\times v_x'^2/V_c^2$ in skimming flows. Flow conditions: d_c/h = 1.15, 1.33 & 1.45, double-tip probe (∅= 0.25 mm).

Discussion

The turbulent kinetic energy is directly related to the transport of bubbles and momentum through the boundary layer. The present data showed consistently large turbulent kinetic energy per unit volume for y/d_c < 0.4 which corresponded to C < 0.5 to 0.6 (Fig. 15). Herein the turbulent kinetic energy per unit volume is defined as :

$$\frac{1}{2}\times\rho\times(v_x'^2+v_y'^2+v_z'^2) \qquad (19)$$

where $\rho = \rho_w\times(1-C)$ is the fluid density. In Figure 15, the horizontal axis represents the dimensionless turbulent kinetic energy per unit volume $(1-C)\times v_x'^2/V_c^2$ assuming that

$v_x' \approx v_y' \approx v_z'$, and where V_c is the critical flow velocity.
Basically the turbulent kinetic energy increased with increasing distance from the triangular invert for $y/d_c < 0.3$. Above ($y/d_c > 0.4$), the turbulent kinetic energy decayed very rapidly with increasing distance from the stepped invert (Fig. 15). The present findings tended to highlight that the maximum production of turbulent kinetic energy per unit volume occurred in the intermediate region, for about C = 0.4 to 0.5 where the bubble count rate was maximum. Further some strong dissipation of turbulent kinetic energy per unit volume was observed for C > 0.5, as illustrated in Figure 15 by the rapid decay with increasing distance y for $y/d_c > 0.4$.

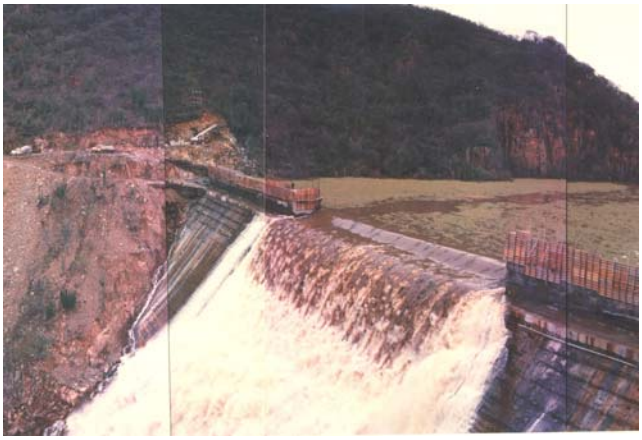

Figure 16: Air-water flow on a prototype stepped spillway: Trigomil dam, Mexico (Courtesy of J.L Sanchez-Bribiesca and F. Gonzalez-Villareal). Flow conditions: Q_w = 1,017 m^3/s, W = 75 m, h = 0.3 m, θ = 51.3º, d_c/h = 8.8, Re = .5.4 E+7.

Self-Similarity in High-Velocity Air-Water Flows

In fluid mechanics, many types of flow motion present some form of self-similarity. A self-similar process is one whose spatial distribution of properties at various times can be obtained from one another by a similarity transformation (Barenblatt 1996). Self-similarity is a powerful tool in turbulence flow research, and high-velocity air-water flows on a stepped chute are one such type of turbulent flow motion involving a wide range of spatial and temporal scales. The non-linear interactions between vortices and entrained air/water particles at different scales lead usually to a complex gas-liquid flow structure. Thus relationships at different scales are of crucial significance in understanding and controlling these flows. They play also a major role in comparing analytical, experimental and numerical results as these results are for different geometric scales. In civil engineering, most spillway applications are for prototype flow conditions with flow Reynolds numbers between 1 E+6 and more than 1 E+9 that cannot be modelled numerically nor physically (Fig. 1B & 16).
Herein, self-similarity was observed in terms of the distributions of air-water flow properties. Table 4 summarises some basic self-similarity equations that were observed during the present work. Self-similarity is illustrated for example in Figures 1, 8, 9, 13, 14. These self-similar relationships were observed at both macroscopic and microscopic levels. For example, the distributions of void fraction and interfacial velocity at a macroscopic level; the cross-correlation function and probability distribution functions of particle chords at a microscopic level (Table 4).
Self-similarity is closely linked with dynamic similarity. Wood (1991) and Chanson (1997) argued that it is nearly impossible to achieve a true dynamic similarity in small-size models of high-velocity air-water flows because of number of relevant dimensionless parameters. The present experimental results showed a number of self-similar relationships (Table 4) that remain invariant under changes of scale. That is, they have scaling symmetry which led in turn to remarkable application at prototype scales. The present results are very significant because they demonstrate a number of self-similar relationships characterising the air-water flow properties in a complex high-velocity flow. They provide a picture general enough to be used, as a first approximation, to characterise the air-water flow field in similar stepped spillway structures irrespective of the physical scale.

Table 4: Self-similarity of the air-water flow properties in high-velocity skimming flows above a stepped spillway.

Flow property	Equation	Remarks
Void fraction distribution	$C = 1 - \tanh^2(\xi)$ $\xi = K' - \frac{y'}{2 \times D_o} + \frac{(y'-1/3)^3}{3 \times D_o}$	$y' \leq 1$
Air-water velocity distribution	$\frac{V}{V_{90}} = y'^{1/N}$ $\frac{V}{V_{90}} = 1$	$y' \leq 1$ $y' > 1$
Bubble count rate distribution	$\frac{F}{F_{max}} = 4 \times C \times (1-C)$	$0 \leq C \leq 1$
PDF of bubble chords	Log-normal distribution	$C \leq 0.3$
PDF of droplet chords	Log-normal distribution	$0.7 \leq C \leq 0.95$
Advective integral length scale	$\frac{L_{xx}}{(L_{xx})_{max}} = 1.6 \times C^{0.55} \times (1-C)^{0.30}$	$C < 0.97$
Transverse integral length scale	$\frac{L_{xy}}{(L_{xy})_{max}} = 1.75 \times C^{0.57} \times (1-C)^{0.324}$	$0 \leq C \leq 1$
Advective integral time scale	$T/T_{max} = 1.97 \times C^{0.59} \times (1-C)^{0.50}$	$C < 0.97$
Turbulence intensity	$Tu = 0.372 \times \exp\left(8.73 \times \frac{L_{xy}}{h}\right)$	$C < 0.97$

Conclusions

New air-water flow experiments were performed in high-velocity flows on a large stepped channel under controlled flow conditions. The gas-liquid flow measurements were performed with some phase-detection intrusive probes in the highly aerated free-surface flow downstream of the inception point of aeration. A combination of single- and double-tip phase detection probes was used. For some experiments, two identical probe sensors were separated by a known transverse distance, and an advanced signal processing technique was developed

with new signal correlation analyses. The results gave some information on the integral length and time scales of the large vortical structures advecting the air bubbles and the air-water structures.

The high-velocity air-water flow properties presented some basic characteristics that were qualitatively and quantitatively in agreement with previous studies. These included the distributions of void fraction, bubble count rate and turbulent interfacial velocity. The auto- and cross-correlation analyses yielded a characterisation of the large eddies advecting the bubbles: i.e., the transverse integral turbulent length and time scales. The turbulent length scales were closely linked with the sizes of the large coherent structures and their interactions with entrained air bubbles. The transverse integral turbulent length scales were related to the step height: i.e., $L_{xy}/h \sim 0.02$ to 0.2, and the integral turbulent time scales were within $0.004 \leq T \times \sqrt{g/h} \leq 0.04$. The results were irrespective of the Reynolds numbers within the range of the experiments.

The present findings showed that turbulent dissipation by large-scale vortices may be a significant process in the intermediate zone defined as ($0.3 < C < 0.7$). The measurements showed some relatively good correlation between turbulence intensities Tu, and turbulent length and time scales (Fig. 14). They highlighted further some maximum turbulence intensities, and maximum integral time and length scales in the intermediate region between the spray and bubbly flow regions (i.e. $0.3 < C < 0.7$). The production of turbulent kinetic energy per unit volume was further maximum in the intermediate region.

Some self-similar relationships were observed systematically at both macroscopic and microscopic levels (Table 4). Although it is nearly impossible to achieve a true dynamic similarity in high-velocity free-surface flow because of the number of relevant dimensionless parameters, the experimental results showed a number of self-similar relationships that remained invariant under changes of scale. The present findings are significant because they provide a picture general enough to be used to characterise the air-water flow field in prototype spillways.

Acknowledgements

The writers acknowledge the assistance of Graham Illidge and Clive Booth.

References

Amador, A., Sanchez-Juny, M., and Dolz, J. 2006. Characterization of the Nonaerated Flow Region in a Stepped Spillway by PIV. Journal of Fluids Engineering, ASME, Vol. 128, No. 6, pp. 1266-1273.

Barenblatt, G.I. 1996. Scaling, Self-Similarity, and Intermediate Asymptotics. Cambridge University Press, UK, 386 pages.

Cain, P., and Wood, I.R. 1981a. Instrumentation for Aerated Flow on Spillways. Journal Hydraulic Division, ASCE, Vol. 107, HY11, Nov., pp. 1407-1424.

Cain, P., and Wood, I.R. 1981b. Measurements of Self-aerated Flow on a Spillway. Journal Hydraulic Division, ASCE, 107, HY11, pp. 1425-1444.

Carosi, G., and Chanson, H. 2006. Air-Water Time and Length Scales in Skimming Flows on a Stepped Spillway. Application to the Spray Characterisation. Report No. CH59/06, Div. of Civil Engineering, The University of Queensland, Brisbane, Australia, July, 142 pages.

Chamani, M.R., and Rajaratnam, N. 1994. Jet Flow on Stepped Spillways. Journal of Hydraulic Engrg., ASCE, Vol. 120, No. 2, pp. 254-259.

Chang, K.A., Lim, H.J., and Su, C.B. 2003. Fiber Optic Reflectometer for Velocity and Fraction Ratio Measurements in Multiphase Flows. Rev. Scientific Inst., Vol. 74, No. 7, pp. 3559-3565. Discussion : 2004, Vol. 75, No. 1, pp. 284-286.

Chanson, H. 1994. Hydraulics of Nappe Flow Regime above Stepped Chutes and Spillways. Australian Civil Engineering Transactions, Institution of Engineers, Australia, Vol. CE36, No. 1, Jan., pp. 69-76.

Chanson, H. 1995. Hydraulic Design of Stepped Cascades, Channels, Weirs and Spillways. Pergamon, Oxford, UK.

Chanson, H. 1997. Air Bubble Entrainment in Free-Surface Turbulent Shear Flows. Academic Press, London, UK.

Chanson, H. 1997b. Air Bubble Entrainment in Open Channels. Flow Structure and Bubble Size Distributions. International Journal of Multiphase Flow, Vol. 23, No. 1, pp. 193-203.

Chanson, H. 2001. The Hydraulics of Stepped Chutes and Spillways. Balkema, Lisse, The Netherlands, 418 pages.

Chanson, H., and Gonzalez, C.A. 2004. Interactions between Free-surface, Free-stream Turbulence and Cavity Recirculation in Open Channel Flows: Measurements and Turbulence Manipulation. Proc. 5th International Conference on Multiphase Flow, Yokohama, Japan, Y. Matsumoto, K. Hishida, A. Tomiyama, K. Mishima and S. Hosokawa editors, Paper 104, 14 pages (CD-ROM).

Chanson, H., and Toombes, L. 2002. Air-Water Flows down Stepped chutes: Turbulence and Flow Structure Observations. International Journal of Multiphase Flow, Vol. 28, No. 11, pp. 1737-1761.

Chanson, H., and Toombes, L. 2004. Hydraulics of Stepped Chutes: the Transition Flow. Journal of Hydraulic Research, IAHR, Vol. 42, No. 1, pp. 43-54.

Gonzalez, C.A. 2005. An Experimental Study of Free-Surface Aeration on Embankment Stepped Chutes. Ph.D. thesis, Department of Civil Engineering, The University of Queensland, Brisbane, Australia, 240 pages.

Gonzalez, C.A., and Chanson, H. 2004. Interactions between Cavity Flow and Main Stream Skimming Flows: an Experimental Study. Canadian Journal of Civil Engineering,

Vol. 31, No. 1, pp. 33-44.

Hayes, M.H. 1996. Statistical, Digital Signal Processing and Modeling. John Wiley, New York, USA.

Herringe, R.A., and Davis, M.R. 1974. Detection of Instantaneous Phase Changes in Gas-Liquid Mixtures. Journal. of Physics E: Scientific Instruments, Vol. 7, pp. 807-812.

Horner, M.W. (1969). An Analysis of Flow on Cascades of Steps. Ph.D. thesis, Univ. of Birmingham, UK, May, 357 pages.

Hoyt, J.W., and Sellin, R.H.J. 1989. Hydraulic Jump as 'Mixing Layer'. Journal of Hydraulic Engineering, ASCE, Vol. 115, No. 12, pp. 1607-1614.

Jones, O.C., and Delhaye, J.M. 1976. Transient and Statistical Measurement Techniques for two-Phase Flows: a Critical Review. Intl Jl of Multiphase Flow, Vol. 3, pp. 89-116.

Kokpinar, M.A. 2005. Flow over a Stepped Chute with and without Macro-Roughness Elements. Canadian. Journal of Civil Eng., Vol.. 31, No. 5, pp. 880-891.

Matos, J. 2000. Hydraulic Design of Stepped Spillways over RCC Dams. International Workshop on Hydraulics of Stepped Spillways, Zürich, Switzerland, H.E. Minor & W.H. Hager Editors, Balkema Publ., pp. 187-194.

Ohtsu, I., and Yasuda, Y. 1997. Characteristics of Flow Conditions on Stepped Channels. Proceedings of the 27th IAHR Biennal Congress, San Francisco, USA, Theme D, pp. 583-588.

Rao, N.S.L., and Kobus, H.E. 1971. Characteristics of Self-Aerated Free-Surface Flows. Water and Waste Water/Current Research and Practice, Vol. 10, Eric Schmidt Verlag, Berlin,
Germany.

Toombes, L. 2002. Experimental Study of Air-Water Flow Properties on Low-Gradient Stepped Cascades. Ph.D. thesis, Department of Civil Engineering, The University of Queensland.

Wood, I.R. 1991. Air Entrainment in Free-Surface Flows. IAHR Hydraulic Structures Design Manual No. 4, Hydraulic Design Considerations, Balkema Publ., Rotterdam, The Netherlands, 149 pages.

Internet resources

Air entrainment on chute and stepped spillways :
{http://www.uq.edu.au/~e2hchans/self_aer.html}